Hydrodynamic electron pumping in two-dimensional electron systems as a signature of viscous transport

A. Gupta[1], J. J. Heremans[1*], S. Fallahi[2], and M. J. Manfra[2]
[1]Department of Physics, Virginia Tech, Blacksburg, VA, USA
[2]Department of Physics and Astronomy, Purdue University, West Lafayette, IN, USA

Hydrodynamic effects arising from electron-electron interactions can have a significant influence on transport dynamics in ultra-clean two-dimensional electron systems[1-3] in the solid state. A growing interest in electron hydrodynamics in the solid state has been noted due to the development of new materials systems[4-7]. Hence signatures of this hydrodynamic regime, where the rate of momentum conserving collisions exceed that of momentum relaxing collisions, are increasingly being explored[8-14]. Here, we experimentally study a hydrodynamic pumping phenomenon using a transverse magnetic focusing geometry[15-21], whereby a ballistic electron jet sweeping past a lithographic aperture can extract (pump) electrons from this aperture. This phenomenon highlights the importance of electron-electron interactions and concomitant hydrodynamic phenomena in mesoscopic ballistic transport, delivers an experimentally supported explanation of nonlocal negative resistances observed in transverse magnetic focusing as signatures of the hydrodynamic regime, and indicates that the Coulombic repulsive interaction can result in a net attractive force.

Transverse magnetic focusing (TMF) has been used to study the ballistic nature of carriers in 3D solids[15,16] and in two-dimensional electron systems (2DESs)[17-21]. In the presence of magnetic field B, ballistic carriers injected from a mesoscopic aperture, the injector (i), follow skipping cyclotron orbits of diameter $D_c = 2\hbar k_F/eB$ to focus on a nearby another aperture, the collector (c), as a result of specular reflections from a barrier of length L (the center to center distance between i and c, Fig. 1a). Here k_F represents the Fermi wavevector, e the electron charge, and $\hbar$ Planck's constant. In the case of a 2DES, B is applied normal to the plane of the 2DES (Fig. 1a). TMF spectra are recorded as the voltage developed at c normalized to

injector current (a nonlocal resistance R_f) vs applied B (Fig. 1b). Maxima are observed in the TMF spectrum when $L = nD_c$, where n is an integer (Fig. 1a-b), due to the ballistic jet impinging on c. In addition to these maxima, negative-valued minima in R_f are also often observed[18-20] (Fig. 1b). The origin of this nonlocal negative resistance has fetched various explanations using ballistic transmission coefficient approaches[22-25]. We demonstrate that the negative values of R_f can result from a hydrodynamic effect, identified with *electron pumping* out of the collector aperture[2].

Nonlocal negative resistances are a hallmark of either hydrodynamic or ballistic effects[26]. The present work supports a hydrodynamic origin for the pumping effect, as modeled in Ref. 2 which forms the microscopic theory for our experiments. Ref. 2 employs a Boltzmann equation with an electron-electron (e-e) collision integral in the relaxation time approximation, a formalism that has equivalently recently been applied to electron hydrodynamics[4,8,26] and TMF[20]. In contrast to recent wire-like or constricted geometries[4,6,7,9,10], the TMF setup is an open-flow geometry (no actual width). In a system with very low momentum-relaxing interactions (with phonons, impurities etc.) and hence low damping like ours, an open geometry promotes hydrodynamic effects such as vortices[26]. The TMF phenomenon is visualized as a ballistic jet of electrons injected into i, exchanging momentum with the surrounding electron fluid by e-e interactions and thereby gradually dissipating (Fig. 1c). The partial dissipation of the jet before it reaches c leads to diminished positive maxima with increasing temperature T, as demonstrated later. The momentum exchange can also lead to a decrease in carrier density in the vicinity of the jet and concomitant entrainment of the fluid (Fig. 1d), effectively leading to extraction (pumping)[2] from c, resulting in the negative minima. The momentum exchange indicates an effective kinematic viscosity ν describing the hydrodynamic regime of transport emphasized in recent work[4,6,7,9,10]. To demonstrate the hydrodynamic pumping phenomenon, we employ the experimentally-determined dependence on T of the TMF signal in a semiclassical analysis, supported by the theoretical model based on a Boltzmann equation[2] and the Landauer-Büttiker formalism[27-29].

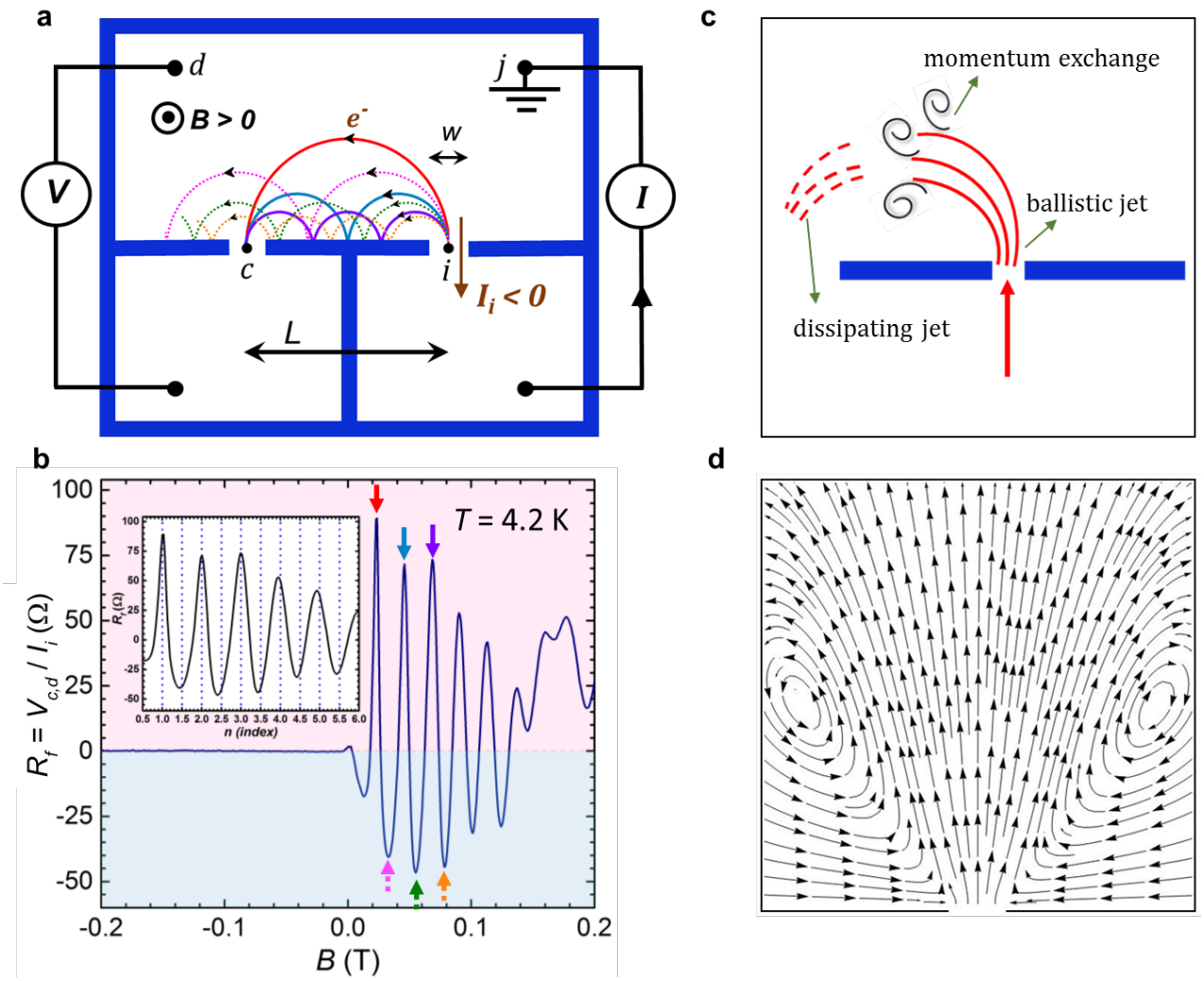

Figure 1| The concept. a, Schematic of TMF setup, with ballistic orbits. **b,** TMF spectra, $R_f = V_{c,d}/I_i$ ($V_{c,d} = V_c - V_d$ and I_i, is the conventional current from *i* to *j* inside the device) vs *B* obtained in experiment on geometry G1 in Fig. 2a). The solid and dotted arrows indicate the maxima and minima respectively, corresponding to the cyclotron orbits of corresponding color in (**a**). For the TMF maxima, orbits impinge directly on *c* and for minima, orbits straddle *c*. The inset depicts data plotted vs index *n* corresponding to $L = nD_c$. Maxima appear at integer *n* and minima at values slightly less than half-integer *n*. The lithographic width of *i* and *c* is 0.8 μm while the actual conducting width w ≈ 0.6 μm due to side depletion. **c,** Schematic of an injected ballistic jet interacting with the surrounding electron fluid by momentum exchange, partially dissipating on its way to *c*. **d,** Streamlines in an illustrative Navier-Stokes simulation of a dissipating jet, entraining the surrounding fluid.

The TMF geometries were patterned on a 2DES in a quantum well in a high-purity GaAs/AlGaAs heterostructure of mobility μ exceeding 740 m^2/s at T = 4.2 K. At the areal electron density $N_S \approx 3.1x10^{15}$ m^{-2}, the Fermi energy $E_F \approx 10.9$ meV. The methods and transport properties are described in Supplementary S1, S2. Experiments were performed on multiprobe Hall mesas on two devices, D1 and D2, bearing four different TMF geometries G1-G4 (Fig. 2a-c). Each TMF geometry features two apertures which can act as injector or collector. Measurements were performed at 4.2 K < T< 20 K, using low frequency lock-in techniques.

An example of main experimental results is depicted in Fig. 1b for G1 (Supplementary S1, S2 for other geometries). The negative-valued R_f are consistent features in all the measurements. As illustrated in Fig. 2d-e, in AC phase-sensitive lock-in voltage detection, a nonlocal negative resistance value indicates that the injected current (from *i*) and the measured voltage (at *c*) are 180^o out-of-phase whereas a positive value indicates they are in-phase. Therefore, the negative value suggests that injection of carriers from *i* (i.e. excess carriers in the injector lead) induces a lack of carriers behind aperture *c*, resulting from carrier extraction (*pumping*) from *c* (Fig.2e). The fact that carrier extraction from *c* can lead to negative R_f is bolstered by a Landauer-Büttiker[27-29] analysis on our system (Supplementary S4).

Nonlocal negative resistances can also occur as a result of ballistic transport without invoking viscous effects, as has been exemplified in ballistic bend resistances and other TMF experiments. Supplementary S5 contrasts the ballistic nonlocal negative resistances with the present viscous pumping effect, and discusses pumping based on the Venturi effect. In short, ballistic nonlocal negative resistances require a special balance between transmission coefficients in the Landauer-Büttiker formalism, whereas viscous pumping is predicted to more generally generate nonlocal negative resistances and is therefore a plausible mechanism.

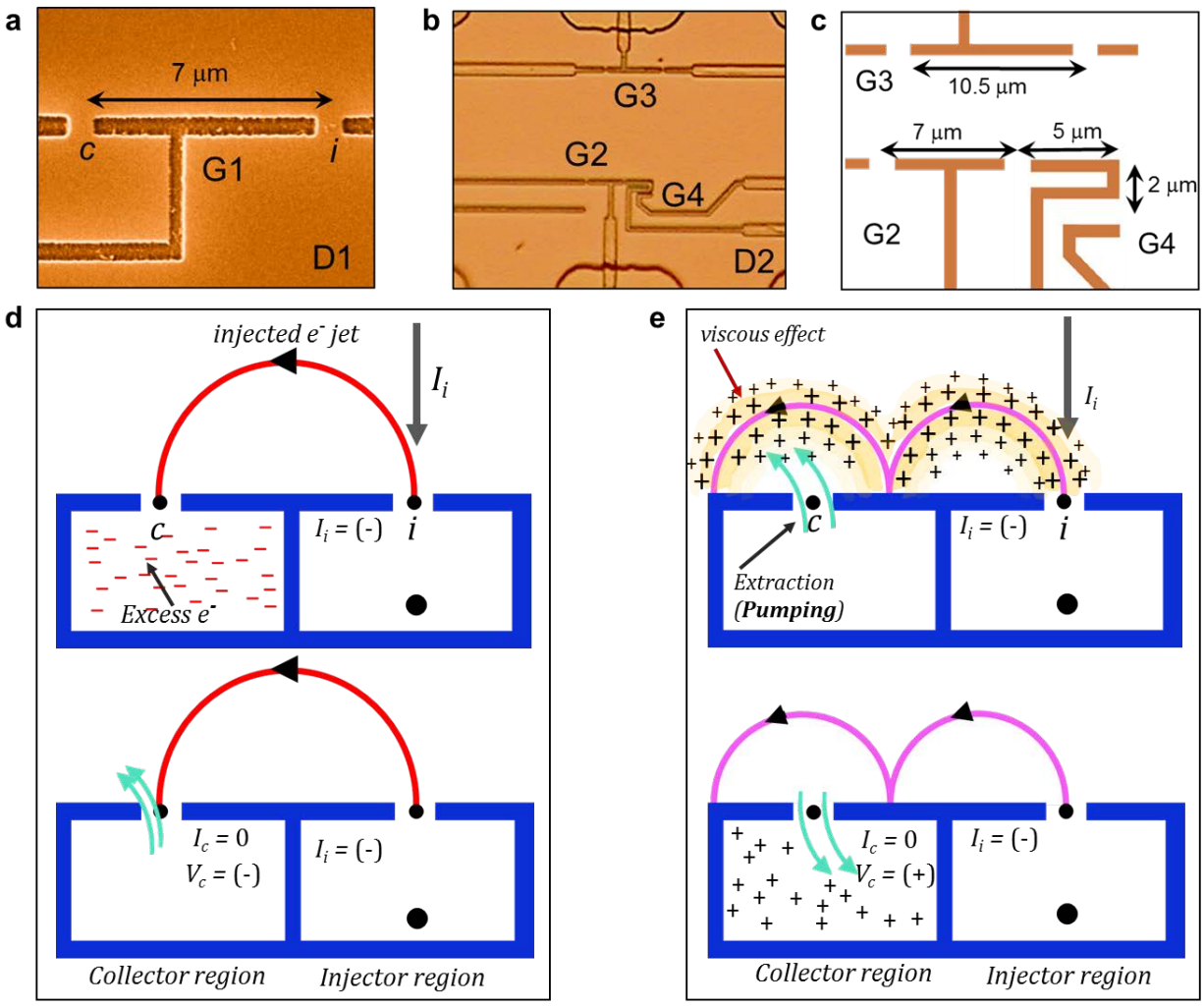

Figure 2| Experimental geometry and origin of signals. a, SEM micrograph of device D1 with geometry G1 representing an inline TMF geometry with *L* = 7 μm pertinent to 1(**b**). **b,c,** Optical image of device D2 with geometries G2, G3 and G4 (relevant dimensions in (**c**)). G2 and G3 represents inline TMF geometries with *L* = 7 μm and 10.5 μm respectively and G4 represents a bent TMF geometry with *L* = 5 μm horizontal and 2 μm vertical (Supplementary S1). **d,** Schematic for a ballistic jet injected from *i* and collected at *c*, leading to excess carrier injection into *c*. Since the collector probe draws no net current, a counter-voltage must be generated behind *c* to expel the excess carriers. The collector aperture then functions similarly to the injector aperture and assumes a voltage of the same sign, leading to nonlocal positive resistance. **e,** Schematic of ballistic jet injected from *i* and straddling over *c*. A net positive charge is developed in the vicinity of the jet due to viscous effects from e-e interactions. Excess electrons from c are extracted (pumped) to compensate for this depletion. Since the collector probe draws no current, a counter-voltage must be generated behind *c* to draw in carriers to compensate for the carrier extraction. The collector aperture then assumes a voltage of opposite sign to the injector, leading to nonlocal negative resistance.

The hydrodynamic regime appears when momentum exchange occurs predominantly between different sections of the carrier fluid rather than with the lattice external to the carrier fluid (with a phonon bath or impurities)[8,11,13]. Momentum exchange within the carrier fluid occurs over a length scale associated with e-e scattering (inelastic but conserving momentum within the carrier fluid), namely $\ell_{ee} = v_F \tau_{ee}$, where τ_{ee} represents the inelastic e-e scattering time[2,4,5,8,12] and v_F the Fermi velocity (Supplementary S6). The scale ℓ_{ee} can be interpreted as a region around the ballistic jet within which the jet exchanges momentum with the surrounding fluid and entrains the fluid[2]. Momentum dissipation out of the fluid occurs over $\ell_e = v_F \tau_e$, where τ_e denotes the electron momentum relaxation time derived from mobility, and ℓ_e is the Drude mobility mean-free-path (Supplementary S1, S6). The kinematic viscosity ν denotes the diffusion coefficient for momentum, and is calculated as $\nu = v_F \ell_{ee} / 4$ [5,10,11]. Hydrodynamic effects induced by ν include the pumping effect[2], the Gurzhi effect in GaAs/AlGaAs channels[4,7], superballistic flow in graphene[6], and formation of vortices in graphene mesoscopic geometries[9,10].

The Boltzmann equation with e-e interactions can under conditions of fast relaxation times be approximated by Navier-Stokes equations for viscous flow[4,8,9,11-14]. As an illustration, the carrier flow field in Fig. 3 was obtained by solving Navier-Stokes equations (Supplementary S7) in a geometry similar to Ref. 2, to show that the pumping effect indeed can be attributed to a viscosity. In the Navier-Stokes approximation of Fig. 3, the ballistic jet is replaced by boundary conditions dictating an injected flow velocity at *i* and extracted at *c* (Ref. 2 contains the rigorous microscopic theory and illustrations). Figure 3a depicts the streamlines in the vicinity of *c*. Figure 3b depicts electrical potential profiles in the carrier fluid. The potential profiles bear a close resemblance to the carrier density variation profiles obtained in Ref. 2. They are related to the latter by the linear relation between carrier density and potential since in a 2DES, a local net charge density will lead to a local potential of the same sign. The regions of negative potential in Fig. 3a-b hence correspond to regions in which the carrier density is lower than in the absence

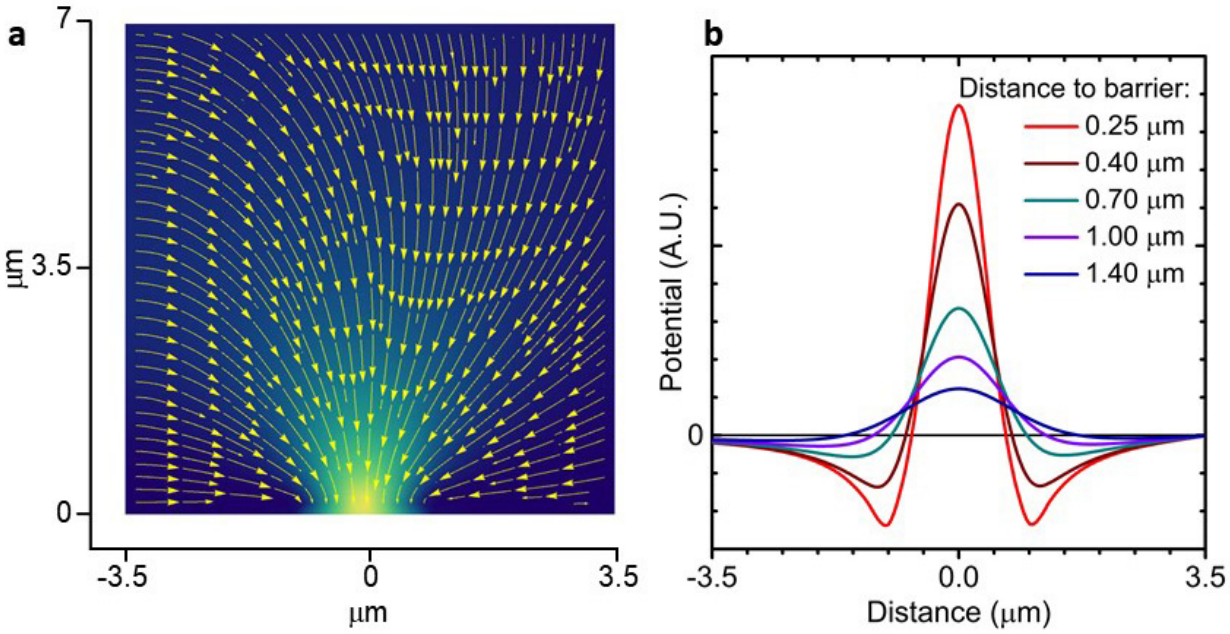

Figure 3| Streamlines and potential profile in a Navier-Stokes approximation. a, Carrier flow streamlines and current density magnitude (color) in the vicinity of *c*, when the current is extracted at *c* and injected at *i* (situated 7 μm to the left to simulate $L = D_c = 7$ μm), calculated with $\nu = 0.5$ m^2/s and $\ell_{ee} = 8.7$ μm, corresponding to $T = 5.6$ K. **b,** Electrical potential profiles in the carrier fluid in the vicinity of *c*. It is apparent that close to the barrier, a region of negative electrical potential develops, extending from ~ 1 μm to almost 3 μm from the center of *c*. In the direction normal to the barrier the negative potential region extends up to ~ 1 μm from the barrier into the carrier fluid.

of an injected jet and hence from which carrier extraction occurs. Figure 3 reconfirms that a viscosity originating in e-e interactions can produce carrier extraction by an injected carrier beam. Figure 2 and Fig. 3 in conjunction can be used to understand the pumping effect in a TMF geometry.

An analysis of the dependence on *T* of TMF spectra[20] helps discern the dominant mechanisms for jet dissipation and for the carrier pumping effect. Fig. 4a-b depict TMF spectra after subtracting a smooth background (Supplementary S3) for G2 and G4 respectively at different *T*. We note that the first maximum for G4 is quite small compared to G2 (Fig 4a-b), attributable to the bent vs in-line geometry. Fig 4c-d contain the TMF amplitude ΔR_f (defined in the insets of Fig. 4c-d) vs *T* for the first maximum in G2 and the

second in G4. We can interpret the decay of ΔR_f as $\Delta R_f = R_o \exp(-\tau_{tr}/\tau)$ where $\tau^{-1}(T)$ is the decay rate of ΔR_f, τ_{tr} is the traversal time and R_o is the value of TMF amplitude in the absence of scattering. We fit the data using $\tau^{-1}(T) \sim T^2 \ln(E_F/k_B T)$ for e-e interactions (Supplementary S8; k_B is the Boltzmann constant) and obtain an excellent fit (Fig. 4c-d). For a cyclotron orbit, the average path length between *i* and *c* is $\pi L/2$, leading to $\tau_{tr} = \pi L/2v_F$. The value of R_o can be obtained from Fig. 4c-d. (Supplementary S8). Figs 4e-f depict the dependence on *T* of $\tau^{-1}(T)$ and of decay length $\ell(T)$, extracted from experimental data using the expression $\tau^{-1}(T) = -\frac{2v_F}{\pi L} \ln \frac{\Delta R_f}{R_o}$ and $\ell(T) = v_F \tau(T)$. A very good agreement with the theoretical $\tau_{ee}^{-1}(T)$ and $\ell_{ee}(T)$ is observed for $\tau^{-1}(T)$ and $\ell(T)$, providing strong evidence that e-e interactions assume a central role in our system. Fig. 4g-h contain the dependence on *T* of the positive maxima ΔR_b and Fig. 4i-j of the negative minima ΔR_p (defined in the insets), and show that ΔR_b and ΔR_p also decay exponentially with $\tau^{-1}(T) \sim T^2 \ln(E_F/k_B T)$. The hydrodynamic carrier extraction effect requires a well-defined ballistic jet, and e-e interactions exchange momentum and impart the jet's momentum to the surrounding carrier fluid, expressed by ν. The existence of a well-defined jet is quantified by ΔR_b. Exchange of momentum inevitably leads to a dissipation of the net momentum of the jet. We then expect that ΔR_b would depend on $\ell_{ee}(T)/L$ (expressing loss of jet momentum by momentum exchange with the surrounding carrier fluid) with the exponential decay dependence confirmed in Fig. 4g-h. Since stronger e-e interactions at higher *T* don't allow the persistence of a well-defined jet over long distances, both the TMF maxima ΔR_b and the pumping minima ΔR_p weaken at higher *T*. The requirement of e-e interactions for viscous momentum exchange on one hand and the dissipation of the ballistic jet by the same e-e interactions on the other, lead to an expression[6] for ΔR_p in terms of additive nonlocal conductances:

$$\frac{1}{\Delta R_p} \sim \frac{1}{\Delta R_b} + \frac{1}{\Delta R_\nu} \qquad (1)$$

where ΔR_b represents the ballistic contribution of the jet and ΔR_ν the viscous momentum exchange leading to carrier extraction. The exact expressions for ΔR_b and ΔR_ν depend on the nonlocal geometry and

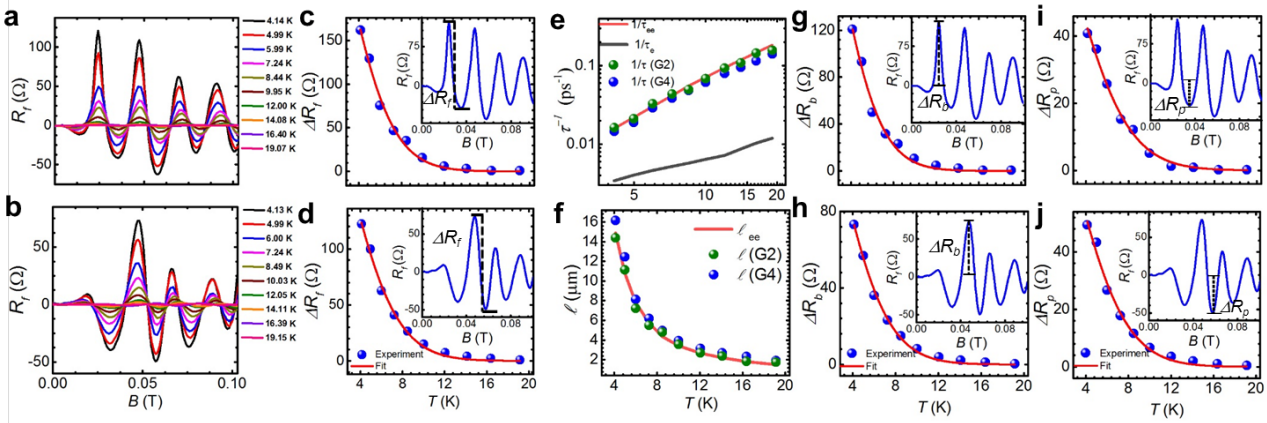

Figure 4|Dependence on *T* of TMF amplitude and role of e-e interactions. a,b, TMF spectra at different *T* for G2 (**a**) and G4 (**b**), 4.2 K < *T* < 20 K after background subtraction. TMF in our system persists to 20 K. **c,d,** TMF amplitude ΔR_f defined in the insets, plotted vs *T* for G2 (**c**) and G4 (**d**). The red solid line represents a fit to exp(-τ_{tr}/τ) with $\tau^{-1}(T) \sim T^2 \ln(E_F/k_BT)$ (Supplementary S8). **e,f,** Decay rate $\tau^{-1}(T)$ and decay length $\ell(T)$, extracted from **c**,**d**. Red solid line in **e** corresponds to theoretical $\tau_{ee}^{-1}(T)$ from Eq. S15 in Supplementary S6; black solid line corresponds to theoretical $\tau_e^{-1}(T)$ (Drude scattering rate) from Eq. S16 in Supplementary S6. Red solid line in **f** denotes the theoretical $\ell_{ee}(T) = v_F\,\tau_{ee}(T)$. **g,h,** Positive maxima ΔR_b defined in the insets, plotted vs *T* for G2 (**g**) and G4 (**h**), showing an exponential decay with $\tau^{-1}(T) \sim T^2 \ln(E_F/k_BT)$. **i,j,** Negative minima ΔR_p defined in the insets, plotted vs *T* for G2 (**i**) and G4 (**j**), showing an exponential decay with $\tau^{-1}(T) \sim T^2 \ln(E_F/k_BT)$.

need further theoretical considerations. It is expected that ΔR_v would predominantly depend on ℓ_{ee}/L with the exponential decay dependence mentioned for Fig. 4i-j. With ΔR_b following the exponential decay confirmed in Fig. 4g-h, we indeed observe that ΔR_p depends on ℓ_{ee}/L according to the expected exponential decay (Fig. 4i-j) in accordance with Eq. 1. In graphene[20], it is also observed that e-e interactions determine the TMF amplitude.

To conclude, hydrodynamic signals appear in TMF, adding to the ballistic phenomena previously thought dominant. Hydrodynamic effects arising from electron-electron interactions can lead to electron pumping, yielding a nonlocal negative resistance in the TMF spectra. The observation that the nonlocal

negative resistance appears in various TMF geometries and that its dependence on temperature tracks electron-electron interactions, both strengthen its plausible interpretation as a signature of hydrodynamic transport.

Methods

The geometries G1-G4 were patterned by gently wet etching in $H_2SO_4/H_2O_2/H_2O$ solution after electron-beam lithograph, using PMMA as etching mask, of the GaAs/AlGaAs heterostructure to a depth removing the GaAs quantum well hosting the 2DES. Prior to electron-beam lithography, a Hall mesa was defined by photolithography and wet etching in the same solution. Ohmic contacts were annealed InSn. Measurements were performed at 4.2 K < T< 20 K in a sample-in-exchange-gas system, using low frequency (~ 45 Hz) lock-in techniques under AC current bias. The transport properties of the unpatterned material were independently characterized on a sample in the van der Pauw geometry using the same methods but omitting lithography steps.

Code availability: the Navier-Stokes equations were numerically solved using Mathematica (Wolfram Research, Inc.) code. The code is available from the corresponding author upon reasonable request.

Data availability

The data that support the plots within this paper and other findings of this study are available from the corresponding author upon reasonable request.

References

1. Gurzhi, R. N. Hydrodynamic effects in solids at low temperature. *Sovi. Phys. Uspekhi* **11,** 255 (1968).
2. Govorov, A. O. & Heremans, J. J. Hydrodynamic effects in interacting Fermi electron jets. *Phys. Rev. Lett.* **92,** 26803 (2004).
3. de Jong, M. J. M & Molenkamp, L. W. Hydrodynamic electron flow in high-mobility wires. *Phys. Rev. B.* **51,** 13389 (1995).
4. Moll, P. J. W., Kushwaha, P., Nandi, N., Schmidt, B. & Mackenzie, A. P. Evidence for hydrodynamic electron flow in $PdCoO_2$. *Science* **351,** 1061 (2016).
5. Lucas, A. & Fong, K. C. Hydrodynamics of electrons in graphene. *J. Phys. Cond. Matter* **30,** 053001 (2018).
6. Kumar, R. K. *et al.* Superballistic flow of viscous electron fluid through graphene constrictions. *Nature Physics* **13**, 1182 (2017).
7. Gusev, G. M., Levin, A. D., Levinson, E. V. & Bakarov, A. K. Viscous electron flow in mesoscopic two-dimensional electron gas. *AIP Advances* **8,** 025318 (2018).
8. Alekseev, P. S. Negative magnetoresistance in viscous flows of two-dimensional electrons. *Phys. Rev. Lett.* **117,** 166601 (2016).
9. Bandurin, D. A. *et al.* Negative local resistance caused by viscous electron backflow in graphene. *Science* **351,** 1055 (2016).
10. Levitov, L. & Falkovich, G. Electron viscosity, current vortices and negative non local resistance in graphene. *Nature Physics* **12**, 672 (2016).
11. Guo, H., Ilseven, E., Falkovich, G. & Levitov, L. Higher-than-ballistic conduction of viscous electron flows. *Proc. Natl Acad. Sci. USA* **114,** 3068 (2017).
12. Scaffidi, T., Nandi, N., Schmidt, B., Mackenzie, A. P. & Moore J. E. Hydrodynamic electron flow and Hall viscosity. *Phys. Rev. Lett.* **118,** 226601 (2017).
13. Torre, I., Tomadin, A., Geim, A. K. & Polini, M. Nonlocal transport and the hydrodynamic shear viscosity in graphene. *Phys. Rev. B* **92,** 165433 (2015).
14. Berdguyin, A. I., *et al*. Measuring Hall viscosity of graphene's electron fluid. *Science* **364,** 6436 (2019).
15. Tsoi, V. S. Focusing of electrons in a metal by a transverse magnetic field. *JETP Lett.* **19**, 70 (1974).
16. Tsoi, V. S., Bass J. & Wyder P. Transverse electron focusing as a way of studying surface crystallography. *Adv. Phys.,* **41,** 365(1992).
17. van Houten, H. *et al.* Coherent electron focusing with quantum point contacts in a two-dimensional electron gas. *Phys. Rev. B* **39**, 8556 (1989).

18. Heremans, J. J., Santos, M. B. & Shayegan M. Observation of magnetic focusing in two-dimensional hole systems. *Appl. Phys. Lett.* **61,** 1652 (1992).
19. Taychatanapat, T., Watanabe, K., Taniguchi, T. & Herrero, P. J. Electrically tunable transverse magnetic focusing in graphene. *Nature Physics* **9**, 225 (2013).
20. Lee, M. et al. Ballistic miniband conduction in a graphene superlattice. *Science* **353**, 1526 (2018).
21. Heremans, J. J. & von Molnar, S. Ballistic electron focusing by elliptic reflecting barriers. *Appl. Phys. Lett.* **74,** 1281 (1999).
22. Büttiker, M. Negative resistance fluctuations at resistance minima in narrow quantum hall conductors. *Phys. Rev. B.* **38,** 12724(R) (1988).
23. Beconcini, M. *et al*. Scaling approach to tight-binding transport in realistic graphene devices: The case of transverse magnetic focusing. *Phys. Rev. B* **94**, 115441 (2016).
24. Milivanovic, S. P., Masir, M. R., Peeters, F. M. Magnetic electron focusing and tuning of the electron current with p-n junctions. *Journal of Applied Physics* **115**, 043719 (2014).
25. LaGasse, S. W. & Lee, J. U. Understanding magnetic focusing in graphene p−n junctions through quantum modeling. *Phys. Rev. B* **95**, 155433 (2017).
26. Chandra, M., Kataria G., Sahdev, D. & Sundararaman, R. Hydrodynamic and ballistic AC transport in two-dimensional Fermi liquids. *Phys. Rev. B* **99**, 165409 (2019).
27. Büttiker, M. Four terminal phase coherent conductance. *Phys. Rev. Lett.* **57,** 1761 (1986).
28. Datta, S. *Electronic Transport in Mesoscopic System* (Cambridge University Press, Cambridge, 1995).
29. Ferry, D. & Goodnick, S. M. *Transport in Nanostructures* (Cambridge University Press, Cambridge, 1997).

Acknowledgements

A.G. and J. J. H acknowledge support by the U.S. Department of Energy, Office of Basic Energy Sciences, Division of Materials Sciences and Engineering under Award DE-FG02-08ER46532, for the conceptualization of the experiments, device fabrication, measurements, data analysis and interpretation. The MBE growth and transport measurements at Purdue are supported by the U.S. Department of Energy, Office of Basic Energy Sciences, Division of Materials Sciences and Engineering under Award No. DE-SC0006671.

Author contributions

A. G. and J. J. H contributed the conceptualization of the experiments, data analysis and interpretation. A. G. performed the device fabrication and measurements. S. F. and M. J. M. provided the MBE-grown high-mobility GaAs/AlGaAs heterostructure. A. G. and J. J. H. composed the manuscript.

Competing interests

The authors declare no competing financial interests.

Materials & correspondence

* Correspondence to J. J. Heremans.

Supplementary Material
to "Hydrodynamic electron pumping in two-dimensional electron systems as a signature of viscous transport"

A. Gupta[1], J. J. Heremans[1], S. Fallahi[2], and M. J. Manfra[2]
[1]Department of Physics, Virginia Tech, Blacksburg, VA, USA
[2]Department of Physics and Astronomy, Purdue University, West Lafayette, IN, USA

S1. Device fabrication and materials properties

The mesoscopic geometries were patterned using electron beam lithography followed by wet etching of the barriers, using PMMA as the etching mask. Two devices, D1 and D2, were fabricated from the same GaAs/AlGaAs MBE-grown material hosting the two-dimensional electron system (2DES) (Fig. 2a-c main text). D1 features a regular in-line transverse magnetic focusing (TMF) geometry G1 with distance between injector and collector L = 7 μm. D2 features three TMF geometries. G2 is a regular in-line TMF geometry with L = 7 μm, G3 is a regular in-line TMF geometry with L = 10.5 μm and G4 is a bent TMF geometry with L = 7 μm (5 μm in horizontal and 2 μm in vertical direction) (Fig. 2c main text). The geometries stand clear of mesa edges or etched barriers that in 2DESs with long mean-free-paths can yield spurious signals from ballistic and/or quantum-coherent transport, ruling out out the possibility that the nonlocal negative resistances occur due to unintended geometrical properties[1].

The van der Pauw method was used to characterize electron transport properties of the unpatterned 2DES in the MBE-grown GaAs/AlGaAs heterostructure, obtaining areal electron density N_S, 2D resistivity $R_\square$, and electron mobility μ. At temperature T = 4.2 K, it is found that $N_S \approx 3.1 \times 10^{15}$ m^{-2}, and $R_\square$ = 2.73 Ω/ □, yielding $\mu \approx 748$ m^2/s (confirming the high purity of the material), Drude (mobility) mean-free-path $\ell_e \approx 68$ μm and Fermi energy, E_F = 10.9 meV (126 K). Here, $\ell_e = v_F\, \tau_e$, where v_F denotes the Fermi velocity and τ_e denotes the Drude momentum relaxation time derived from $\mu = e\,\tau_e/m^*$, where m^* denotes the electron effective mass (0.067 m_e where m_e denotes the free-electron mass) and e the electron charge. Non-parabolicity of the band structure was taken into account in calculating the transport properties[2,3]. N_S increases with increasing T (Fig. S1a) and $R_\square$ as well (Fig. S1b), while $\mu \sim 1/T$ (Fig. S1c), demonstrating that μ is limited by scattering with acoustic phonons as expected. Fig S1d depicts 1/ μ vs T, indicating that $\frac{1}{\mu(T)} = \frac{1}{\mu_o} + \alpha T$, where μ_0 denotes μ limited by impurity scattering and αT describes the linear dependence on T due to acoustic phonon scattering consistent with theory in the equipartition regime (4-40 K)[4]. The Fermi wavelength λ_F = 45 nm, and with conducting aperture width $w \approx 0.6$ μm, it is expected

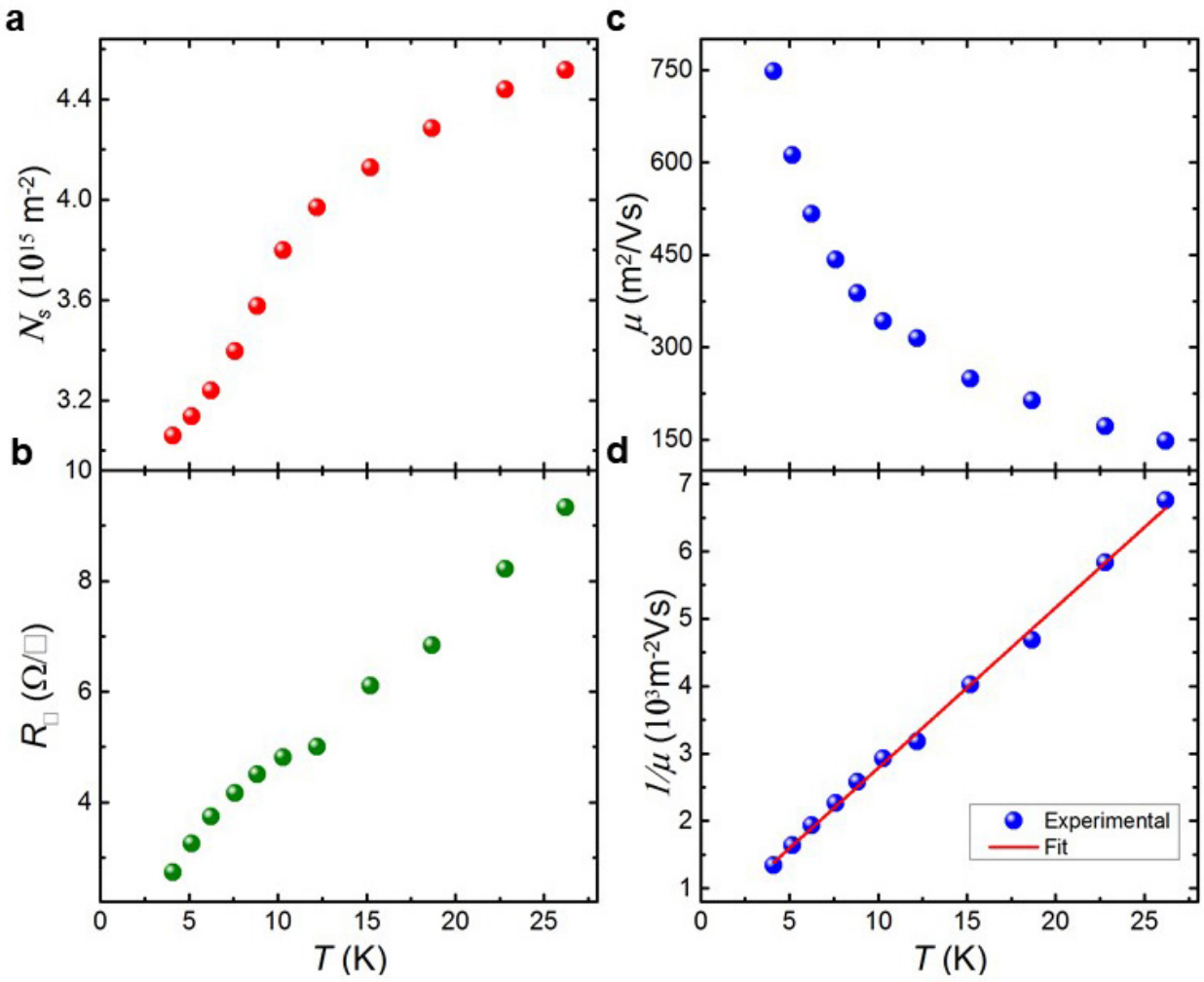

Figure S1| Transport characteristics. a, Carrier density N_S vs T. **b,** 2D resistivity $R_\square$ vs T. **c, d,** μ vs T and $1/\mu$ vs T. From the fit (red curve), we extract the fitting parameters $1/\mu_0$ = 4.07 x 10^{-4} m^{-2}s and α = 2.38 x 10^{-4} m^{-2}sK^{-1}.

that $w/(\lambda_F/2) \approx 27$ modes contribute to transport, a large number indicating that quantized transport through the apertures can be neglected.

S2. Properties of TMF

TMF spectra were obtained by applying a low-frequency AC current with rms amplitude varying from 50 nA to 1 μA between probes *i* (injector) and *j* (faraway current drain) and measuring the voltage developed between probe *c* (collector) and *d* (faraway voltage reference contact; Fig. 1a main text). Contacts *j* and *d* are several ℓ_e (several 100 μm) removed from *i* and *c* and from each other, such that transport between *i*, *c* and *j* and *d* is neither ballistic nor quantum-coherent (transport between *i* and *c* is ballistic and possibly quantum-coherent). Measured $V_c - V_d$ were found to be linear in current amplitude

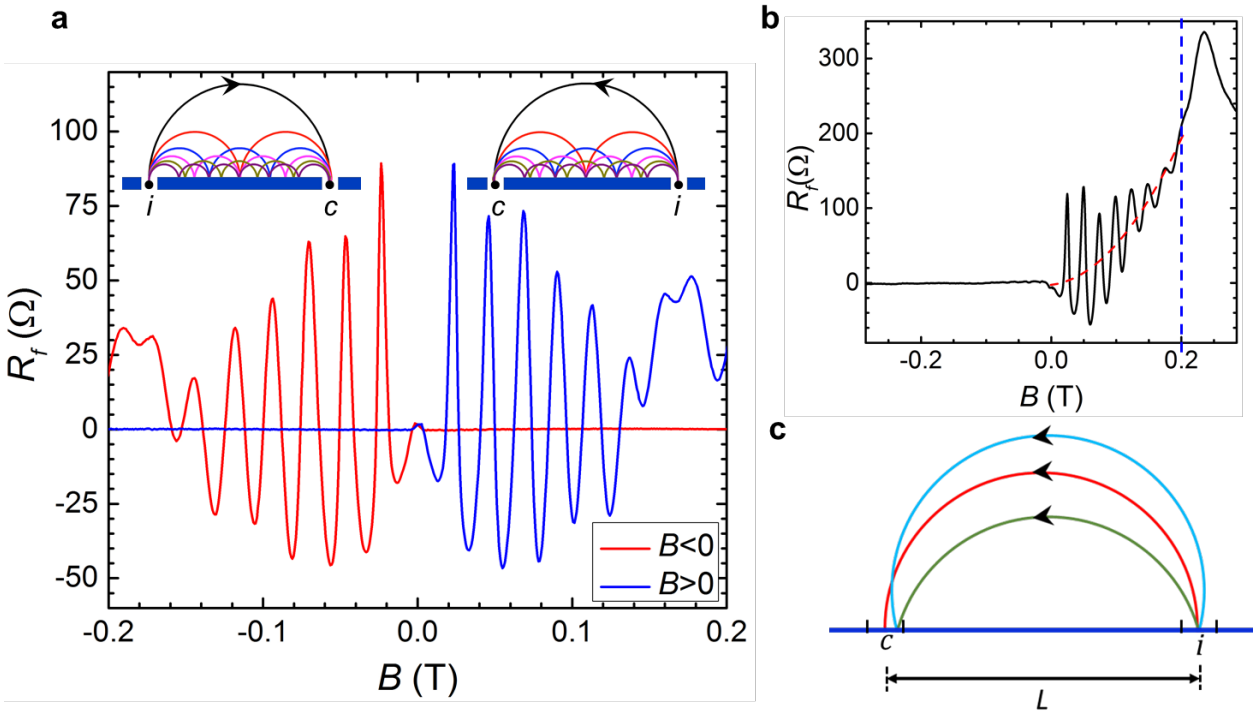

Figure S2| Properties of TMF. a, TMF at T = 4.2 K for G1 when current and voltage contacts are exchanged and polarity of B inverted, illustrating Onsager reciprocity. The insets depict the semiclassical orbits corresponding to the TMF maxima. **b,** TMF at T = 4.2 K for G2 illustrating that the relevant data lies below 0.2 T. The dashed red line shows the rising background magnetoresistance superposed on TMF. TMF maxima and minima are quantified from this magnetoresistance background. **c,** Focusing effect of the TMF geometry, illustrated with the injection angle differing from $\pi/2$ to the barrier (red orbit's injection angle is $\pi/2$ as reference).

up to ~ 400 nA rms, beyond which gradual sublinearity in the characteristic was noted (section S9). To avoid electron heating, measurements discussed in this work were obtained at 100 nA rms.

Due Onsager reciprocal relations[5,6] TMF should be symmetric if the injector and collector are exchanged and the polarity of B inverted. Figure S2a shows an example of this relation for G1. While discrepancies can arise in mesoscopic devices[7], in the present devices these are small, allowing us to show the TMF spectra for only one polarity of B. The cyclotron diameter D_c approaches $w \approx 0.6$ μm at $B \approx 0.3$ T, and hence well-defined semiclassical cyclotron orbits reflecting off the barrier require $B < 0.3$ T. As Fig. S2b illustrates, the relevant data in this work hence occurs for $B \leq 0.2$ T.

Figure S2c illustrates that a cyclotron orbit starting at an angle different from $\pi/2$ to the barrier, will land in the vicinity of c at a distance less than $L = D_c$ from i (illustrated case corresponds to first maximum). However, if the injection angles are not far from $\pi/2$, the orbits undergo magnetic focusing

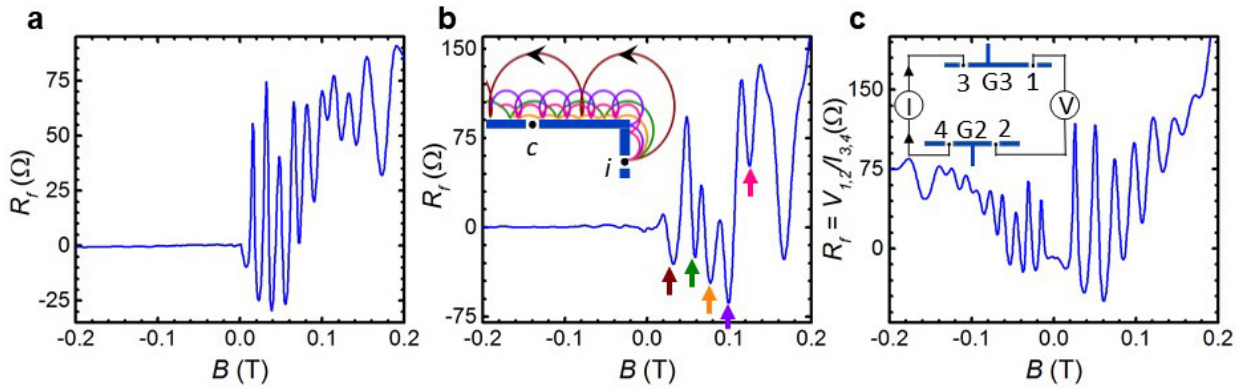

Figure S3| TMF and semiclassical analysis. a, TMF spectrum obtained at T = 4.2 K on G3, showing the commonly observed magnetoresistance background. **b,** TMF spectrum obtained at T = 4.2 K on bent geometry G4, negative TMF minima indicated by arrows. The inset shows simulated semiclassical skipping orbits corresponding to the minima. **c,** Combined TMF spectra for G2 and G3 obtained at T = 4.2 K in the measurement setup depicted in the inset. The TMF spectrum at $B > 0$ corresponds to G2 (L = 7 μm) and at $B < 0$ corresponds to G3 (L = 10.5 μm).

onto *c*, a property due to D_c being an extremal length scale of the cyclotron orbit for a GaAs 2DES. More generally, in a semiclassical approach, under a magnetic field B the path in reciprocal space coincides with cross-sections of the Fermi surface corresponding to equal-energy contours[8,9]. In real space the cyclotron orbit corresponds to a path of the same shape, rotated by 90° and scaled as 1/B. TMF spectra emphasize those orbits corresponding to extremal Fermi surface cross-sections. If the Fermi surface is circular with diameter $2k_F$ (as for a GaAs 2DES), then $D_c = 2\hbar k_F/eB$ (where k_F represents the Fermi wave vector). Carrier reflection from a potential barrier obtained by gentle wet etching is predominantly specular and hence TMF maxima appear when $L = nD_{cn} = 2n\hbar k_f/eB_n$,where n is an integer and B_n is the magnetic field corresponding to the n^{th} maximum (inset in Fig. S2a). In Figs. S2a-b, the TMF amplitude decreases with increasing n >3 and for n > 6 the spectrum loses definition. Two reasons contribute to this effect: 1) as mentioned, at higher B, $D_c \rightarrow w$, leading to a gradual loss of definition in the TMF geometry, and 2) deviations from ideal specular reflection of carriers off the TMF barrier leads to a gradual loss of a well-defined ballistic jet after several skipping events off the barrier.

Figure S2b illustrates the magnetoresistance background often superposed on TMF (dashed red line). Figure S3a shows another examples of TMF and the background magnetoresistance obtained on G3. While the first few minima show $R_f < 0$ in an absolute sense, subsequent minima show R_f below the rising magnetoresistance background but not crossing the $R_f = 0$ line in the graph. Since the magnetoresistance

background occurs independently of the TMF phenomenon (and can have several origins), this background is counted as the reference line and subtracted as discussed in S3.

Figure S3b depicts TMF in the bent geometry G4, with current injected from *i* and voltage detected at *c* as labeled in the inset. Particularly, the fact that the maximally negative TMF features (minima) correspond to cyclotron orbits straddling *c* and nearly reaching their apex over *c* is illustrated. Hence, regarding the circumstances under which maximally negative TMF features occur, both in-line and bent geometries concur.

Due to the positioning of G2 and G3, it is possible to obtain their TMF spectra in a single measurement, as shown in Fig. S3c and its inset depicting the measurement setup. The spectrum due to G2 ($B > 0$) shows a larger amplitude than the spectrum due to G3 ($B < 0$) because $L = 7$ μm in G2 and $L = 10.5$ μm in G3, which further demonstrates the dependence on L of TMF amplitudes.

S3. Background removal

As discussed in S2, a magnetoresistance background occurs independently of the TMF phenomenon. We can remove the background by carefully identifying it with a suitable smoothing filter. In the main text Fig. 4a-b, the background is removed using a LOESS (locally weighted smoothing) filter. We choose the span of the filter such that the amplitudes of the peaks are not much affected (which can be verified by varying the chosen span). After subtracting the smooth background, we subtract a baseline such that at $B = 0$, the resistance is approximately zero.

S4. Landauer-Büttiker analysis

The Landauer-Büttiker formalism provides a framework to describe mesoscopic transport in terms of multiprobe transmission of coherent modes[10-12]. In the presence of dominant inelastic electron-electron scattering, the transmission coefficients cannot strictly be ascribed to coherent modes, yet with proper semiclassical interpretation the formalism provides insight in the role of geometry and of current and voltage probes in the multiprobe TMF measurements. We use the formalism to show that carrier extraction (pumping) from *c* straightforwardly leads to negative-valued R_f without further assumptions or tuning of transmission coefficients.

The linearized current equations can be expressed as[11]:

$$I_j = \frac{2e^2}{h}\sum_k T_{jk}\left(V_k - V_j\right) \qquad (1)$$

I_j represents the net conventional current into the probe *j* (Fig. S4) and T_{jk} the transmission coefficient from *k* to *j* ($T_{j\leftarrow k}$). We consider a 4-probe setup with an injector *i*, collector *c* and and two counter-probes p1 (current drain) and p2 (voltage reference) (Fig. S4). From Eq. (1):

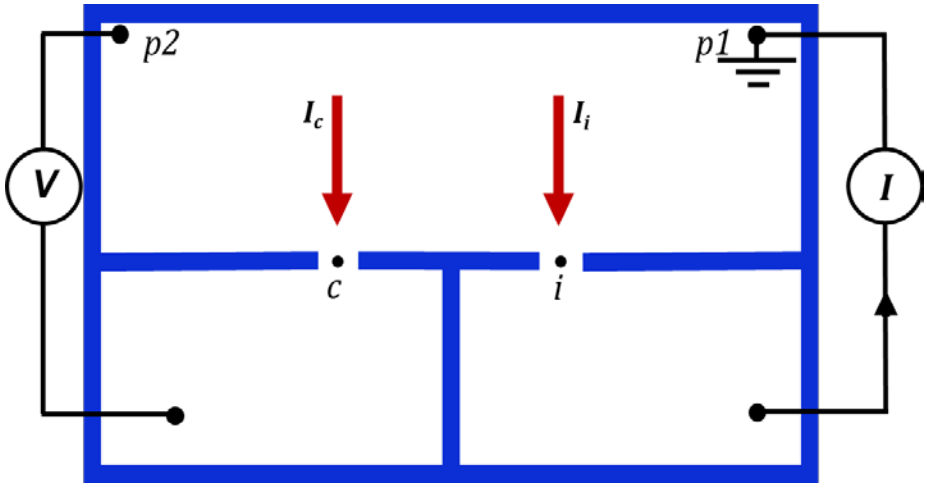

Figure S4| Schematic TMF geometry. A regular 4-probe geometry, featuring injector *i* and collector *c*, two faraway counter-probes p1 and p2. Currents entering into the apertures are considered positive (hence in the present case, applied $I_i < 0$).

$$I_c = \frac{2e^2}{h}\left[T_{ci}(V_i - V_c) + T_{cp1}(V_{p1} - V_c) + T_{cp2}(V_{p2} - V_c)\right] = 0 \quad (2)$$

$$I_i = \frac{2e^2}{h}\left[T_{ic}(V_c - V_i) + T_{ip1}(V_{p1} - V_i) + T_{ip2}(V_{p2} - V_i)\right] < 0 \quad (3)$$

$$I_{p1} = \frac{2e^2}{h}\left[T_{p1c}(V_c - V_{p1}) + T_{p1i}(V_i - V_{p1}) + T_{p1p2}(V_{p2} - V_{p1})\right] \quad (4)$$

$$I_{p2} = \frac{2e^2}{h}\left[T_{p2c}(V_c - V_{p2}) + T_{p2i}(V_i - V_{p2}) + T_{p2p1}(V_{p1} - V_{p2})\right] \quad (5)$$

$I_c = 0$ since *c* represents a voltage contact. To correspond to the actual measurements the formalism requires $I_i < 0$ (Fig. S4). Also, since when TMF occurs, no transmission occurs from *c* to *i*, we have $T_{ic} = 0$. From Eq. 2 and Eq. 3:

$$(V_c - V_{p2})[T_{ci}T_{ip2} + (T_{cp2}(T_{ip1} + T_{ip2})] = -\frac{h}{2e^2}I_i(T_{ci}) - (V_c - V_{p1})[T_{ci}T_{ip1} + (T_{cp1}(T_{ip1} + T_{ip2})] \quad (6)$$

In our geometry, the two counter-probes, p1 and p2 are faraway contacts (many mean free paths away). Hence, it is reasonable to assume $V_{p1} = V_{p2} = V_p$. Entering this into 6, we obtain:

$$V_c - V_p = -\frac{h}{2e^2}I_i\left(\frac{T_{ci}}{(T_{ci} + T_{cp1} + T_{cp2})(T_{ip1} + T_{ip2})}\right)$$

$$R_f = \frac{V_c - V_p}{-I_i} = \frac{h}{2e^2}\left(\frac{T_{ci}}{(T_{ci} + T_{cp1} + T_{cp2})(T_{ip1} + T_{ip2})}\right) > 0 \quad (7)$$

where R_f is the nonlocal TMF resistance and is necessarily positive since $I_i < 0$.

If we assume that p1 and p2 are very far off, we can effectively merge p1 and p2 into a single contact, obtaining an effective 3-probe setup with an injector *i*, collector *c* and and a faraway contact at ∞ (Fig. S5), as a simplification of our actual 4-probe TMF geometry above.

Using $V_{p1} = V_{p2} = V_\infty$, $T_{cp1} + T_{cp2} = T_{c\infty}$ and $T_{ip1} + T_{ip2} = T_{i\infty}$, we obtain:

$$R_f = \frac{V_c - V_\infty}{-I_i} = \frac{h}{2e^2}\left(\frac{T_{ci}}{T_{i\infty}(T_{c\infty} + T_{ci})}\right) > 0 \quad (8)$$

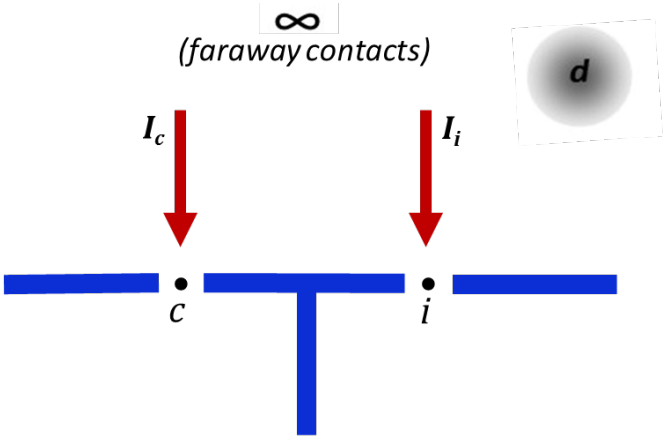

Figure S5| Schematic 3-probe TMF geometry. A 3-probe geometry is derived from Fig. S4 assuming faraway counter-probes (functionally merging into one faraway probe at ∞), injector *i* and collector *c*, a faraway probe, and a region *d*.

Assuming $T_{i\infty} \approx T_{c\infty} = T_\infty$:

$$R_f = \frac{h}{2e^2}\left(\frac{T_{ci}}{T_\infty(T_\infty + T_{ci})}\right) \quad (9)$$

At small T_∞, $R_f \sim \frac{1}{T_\infty}$ and at small T_{ci}, $\frac{dR_f}{dT_{ci}} \sim \frac{1}{T_\infty{}^2}$ (linear in T_{ci}), demonstrating that R_f increases if transmission to and from the faraway counter-probes is diminished.

$R_f \geq 0$ in Eqs. 7 and 8, indicating that the TMF signal cannot assume negative values if the counter-probes are assumed faraway, as they are in the experiments. A negative value requires an additional phenomenon, found below in carrier extraction from *c*.

A new 4th probe *d* is introduced to the effectively 3-probe setup to allow a transmission coefficient T_{dc} describing transmission *out of c* to this 4th probe (carrier extraction from *c*). Probe *d* does not need to represent a physical contact or aperture, but rather can be a region of the 2DES towards which carrier extraction from *c* occurs by the action of the ballistic jet (Fig. S5).

$$I_c = \frac{2e^2}{h}[T_{ci}(V_i - V_c) + T_{c\infty}(V_\infty - V_c) + T_{dc}(V_c - V_d)\,] = 0 \qquad (10)$$

$$I_i = \frac{2e^2}{h}[T_{ic}(V_c - V_i) + T_{i\infty}(V_\infty - V_i) + T_{id}(V_d - V_i)\,] < 0 \qquad (11)$$

From Eqs. 10 and Eq. 11 and, as above, stating $T_{ic} = 0$ yields:

$$(V_c - V_\infty)[T_{c\infty}T_{id} + T_{i\infty}(T_{c\infty} + T_{ci})] = -\frac{h}{2e^2}I_i(T_{ci}) - (V_c - V_d)[T_{ci}T_{id} - T_{dc}(T_{i\infty} + T_{id})] \quad (12)$$

Assuming that *d* is far away and hence at the potential at ∞, such that $V_d = V_\infty$:

$$R_f = \frac{V_c - V_\infty}{-I_i} = \frac{h}{2e^2}\left(\frac{T_{ci}}{(T_{i\infty} + T_{id})(T_{c\infty} + T_{ci} - T_{dc})}\right) \qquad (13)$$

Assuming $(T_{i\infty} + T_{id}) \approx T_{c\infty} = T_\infty$,

$$R_f = \frac{V_c - V_\infty}{-I_i} = \frac{h}{2e^2}\left(\frac{T_{ci}}{T_\infty(T_\infty + T_{ci} - T_{dc})}\right) \qquad (14)$$

Hence with the addition of carrier extraction from *c*, R_f can assume negative values depending on relative value of coefficients. In particular strong carrier extraction from *c*, and hence high T_{dc}, can lead to negative R_f. As *B* is varied, T_{ci} and T_{dc} in particular vary. Positive TMF maxima occur when the ballistic jet impinges in the vicinity of or at *c* (high T_{ci}), and negative minima occur when the ballistic jet straddles *c*, leading to electron pumping (high T_{dc}).

In the Landauer-Büttiker formalism, 4-probe calculations can lead to negative resistances in general, depending on transmission coefficients[13,14]. Yet we stress that, 1) if two faraway counter-probes are assumed as current drain and voltage reference, which is a realistic approximation of our geometry, then without explicit carrier extraction from *c*, R_f will be positive, and 2) if in the same geometry carrier extraction from *c* is introduced as only additional assumption, then R_f can assume negative values if carrier extraction is sufficiently pronounced. Hence, electron pumping emerges as a strong explanation for negative R_f.

We add that in a 4-probe measurement, resistance should assume the form[12] $R_{4t} = \frac{h}{2e^2}\frac{1-T}{T}$. However, 1-$T \approx 1$ if T is small. Experimentally the substitution would not contribute a noticeable difference if the device including the counter-probes extends over many mean free paths[11], as is the present case.

S5. Differences with other effects

Nonlocal negative resistances can have a ballistic or a hydrodynamic origin. Here we discuss ballistic effects and contrast them with the carrier pumping effect of hydrodynamic origin.

Bend resistance

In the ballistic bend resistance geometry[15-17], in a 4-probe geometry a voltage-probe collector is placed adjacent to the current-probe injector, along a bend between injector and collector. At $B \approx 0$, the ballistic jet travels straight on, fails to negotiate the bend and fails to transmit to the collector. A sharp nonlocal negative resistance at $B = 0$ results, contrary to expectations of a diffusive picture in which the current will negotiate the bend. In TMF however, the collector is not placed along a bend relative to the injector and when the collector receives the ballistic beam (i.e. focusing) a positive nonlocal resistance maximum results, not negative. Instead, nonlocal negative resistance at specific values of $B \neq 0$ result from net extraction of charge, or from specific choices of transmission coefficients if all four probes support coherent transmission between each other.

Venturi electron pumping

A pumping effect based on Venturi effect[18] in fluid dynamics has been demonstrated, with a mechanism different from viscous entrainment. The Venturi effect is based on Bernoulli's equation (conservation of energy), where the pressure variations are quadratic in velocity (via kinetic energy) and, thus quadratic in current. The present pumping effect, on the other hand, is linear in applied voltage or current[19] (cfr S9) is based on a quantum-mechanical description of electron-electron interactions, and is understood from viscous effects (effectively Newton's 2nd law).

Landauer-Büttiker formalism (coherent)

The Landauer-Büttiker formalism can give rise to nonlocal negative four-probe resistances in TMF without using the extraction term in S4[13,14] However, it is important to note that in previous Landauer-Büttiker TMF descriptions the current and voltage counter-probes were assumed to be in close proximity to the injector and collector probes such that coherent transmission was a physically

reasonable assumption between all four probes. Then, by specific choices transmission coefficients (e.g. higher magnitude of transmission coefficient from injector to a far-away contact as compared to that from injector to collector) negative resistances can be obtained. In our geometry, the current and voltage counter-probes are far away (up to millimeters) so coherent transmission between the counter-probes and the injector and collector probes is simply unlikely. As we have shown in S4, in contrast the hydrodynamically plausible scenario of carrier extraction from the collector straightforwardly and generally yields negative four-probe resistances, without the assumption of nearby counter-probes and special transmission coefficients. The simple implementation of carrier extraction from the collector, expressed using a new transmission coefficient out of the collector, immediately leads to nonlocal negative four-probe resistances in TMF without further assumptions. In short, while the Landauer-Büttiker formalism can certainly give rise to nonlocal negative four-probe resistances in TMF in special cases, we show that a hydrodynamically plausible more general scenario may be a more reasonable explanation in our geometry.

S6. Calculation of different length scales

The hydrodynamic regime materializes when momentum exchange of the carriers occurs chiefly within the carrier fluid (preserving momentum within the fluid) rather than with external entities (the lattice, e.g. phonon baths or impurities)[20-22]. The momentum exchange within the carrier fluid occurs via electron-electron (e-e) interactions, occurring over a length scale ℓ_{ee}, where $\ell_{ee} = v_F\ \tau_{ee}$ with τ_{ee} the inelastic e-e scattering time. Momentum relaxation out of the carrier fluid occurs over the length scale of the Drude mean-free-path $\ell_e = v_F\ \tau_e$ (cfr S1). Momentum exchange between layers of the carrier fluid leads to a kinematic viscosity, as $\nu = v_F\ \ell_{ee} / 4$ [21,23,24]. The expression for ν is closely reminiscent of the expression derived in the kinetic theory of gases and ℓ_{ee} can be regarded as the average diffusion length for momentum in the fluid. Apart from ℓ_{ee} and ℓ_e, another relevant length scale is L, characterizing the device size[25-27].

The scattering rate from inelastic e-e scattering, $1/\tau_{ee}$, is given as [19,28]:

$$\frac{1}{\tau_{ee}(T)} = \frac{(k_B T)^2}{hE_F}\left[\ln\frac{E_F}{k_B T} + \ln\frac{4}{a_o^* k_F} + 1\right] \qquad (15)$$

where E_F, k_F, a_o^* and k_B are the Fermi energy, the Fermi wave vector, the effective Bohr radius and the Boltzmann constant respectively.

We note that a *T*-independent part of the scattering rate describing momentum exchange which also preserves total momentum within the fluid can be considered, as:

$$\frac{1}{\tau_{mc}} = \frac{1}{\tau_{ee}(T)} + \frac{1}{\tau_{mc,o}}$$

where $1/\tau_{mc}$ represents the total momentum-conserving scattering rate and $1/\tau_{mc,o}$ its *T*-independent part, considered to originate from the relaxation of second moment of the electron distribution[20]. In this work we will not include $1/\tau_{mc,o}$.

The rate of momentum relaxation out of the carrier fluid is in the equipartition regime (4-40 K) approximated as[4,20] (cfr S1):

$$\frac{1}{\tau_e} = \frac{1}{\tau_{ph}(T)} + \frac{1}{\tau_{e,o}} \approx A_{ph}T + \frac{1}{\tau_{e,o}} \quad (16)$$

where $1/\tau_{ph}$ represents the phonon scattering rate, A_{ph} a phonon scattering coefficient, and $1/\tau_{e,o}$ the residual scattering rate due to impurities[23].

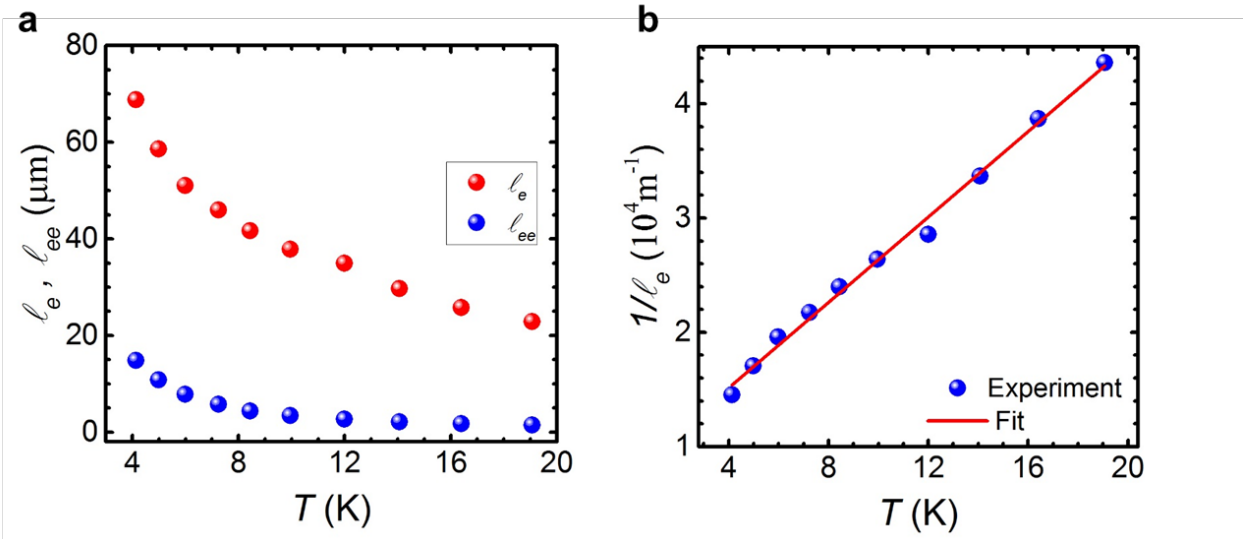

Figure S6| Relevant length scales. a, ℓ_{ee} and ℓ_e comparatively plotted vs *T*. **b,** $1/\ell_e$ plotted vs *T*, demonstrating that Eq. S16 captures the data well.

Fig S6a shows ℓ_e and ℓ_{ee} plotted vs *T* as obtained on the patterned devices. Here ℓ_e was calculated from measurements of N_S and $R_\square$ (cfr S1) and ℓ_{ee} from Eq. 15 using the measurements of N_S. Since $\ell_{ee} < \ell_e$ over the range of *T* of the experiments (Fig. S6a), transport in the 2DES is expected to show hydrodynamic phenomena[25,27]. Since $\ell_e > L$ momentum will not substantially dissipate to the lattice within the device size.

Figure S6b shows that Eq. 16 describes the dependence on T of $1/\tau_e$ well (cfr S1) and shows that acoustic phonon scattering dominates in $1/\tau_e$ in the range of T of the experiments, as expected for a high-purity 2DES. From Fig. S5c and Eq. 16 we extract $A_{ph} \approx 3.5 \times 10^8$ s^{-1}K^{-1} and $\tau_{e,o} \approx 7.1 \times 10^{-10}$ s. We note that e-e scattering, while limiting TMF, does not play a role in determining μ in the 2DES because e-e scattering conserves the total momentum of the carrier fluid and merely causes a redistribution of momentum internally to the fluid. The loss of total momentum of the carrier fluid, here mostly caused by acoustic phonon scattering, is what is quantified in μ.

S7. Navier-Stokes approximation

Figure 3 and Fig. 1d of main text were obtained in a Navier-Stokes approximation, numerically solving two-dimensional Navier-Stokes equations:

$$\left(\vec{v}\cdot\vec{\nabla}\right)\vec{v} = \nu\nabla^2\vec{v} - \left(\frac{e}{m^*}\right)\vec{\nabla}V \qquad (17)$$

where $\vec{v}$ represents the drift velocity in the carrier fluid, and V the electrical potential (ν, e and m^* as above). For the numerical implementation, dimensionless variables are introduced, such that lengths $x \rightarrow \bar{x} = x/L_0$, velocities $v \rightarrow \bar{v} = v/v_0$, the Reynolds number $Re = v_0 L_0/\nu$, and the potential $V \rightarrow \bar{V} = (eV/m^* v_0^2)$, and derivatives are vs the dimensionless lengths. The scales L_0 and v_0 are characteristic scales of the problem. This leads to the dimensionless Navier-Stokes equations:

$$\left(\vec{\bar{v}}\cdot\vec{\bar{\nabla}}\right)\vec{\bar{v}} = \frac{1}{Re}\bar{\nabla}^2\vec{\bar{v}} - \vec{\bar{\nabla}}\bar{V} \qquad (18)$$

We have adopted the choice L_0 = (TMF barrier length)/2 = $L/2$ = cyclotron radius at 1st TMF maximum, and $v_0 = v_F$. We take $\nu = v_F\,\ell_{ee}/4$, and hence the choices lead to $Re = 2L/\ell_{ee}$. In Fig. 3 main text, we assume the values ℓ_{ee} = 8.7 μm (corresponding to T = 5.6 K), and L = 7 μm (the barrier length for the in-line TMF geometries) and we calculate ν = 0.50 m^2/s (similar to honey at room temperature). The choices yield Re = 1.61, effectively corresponding to a viscous flow regime. Figure 3 main text, was obtained with Eq. 18 and above parameters, with no-slip boundary conditions ($\vec{v}$ = 0) at all boundaries. The applicability of strict no-slip boundary conditions is debated for solid-state carrier fluids, and tentative consequences are briefly discussed below. The reference point with V = 0 is taken 14 μm away from the TMF barrier on plumb line to the barrier equidistant to i and j. Figure 1d main text was for illustrative purposes obtained at Re = 108 (lower ν and hence lower momentum transfer to the surrounding fluid).

The Navier-Stokes calculations in Fig. 3 main text are mainly for illustrative purposes. A rigorous microscopic theoretical calculation incorporating both ballistic and hydrodynamic transport is provided

in Ref. 19, which forms the framework for the present experiments. Ref. 19 uses a linearized Boltzmann equation with electron-electron collision integral to provide a microscopic description. A Boltzmann equation is also used in a similar way in Refs. 20, 29-31among others. The Navier-Stokes equations provide a macroscopic description and do not capture the ballistic aspects, whereas a Boltzmann equation provides a microscopic description and can capture both ballistic and hydrodynamic aspects[31] Yet the Navier-Stokes equations can be derived from the Boltzmann equation assuming a short relaxation time (for instance by using a Chapman-Enskog expansion), showing the strong connection between them. The similarity in potential profiles obtained in the Navier-Stokes approximation in Fig. 3b main text and by the rigorous microscopic theoretical description of Ref. 19, Fig. 2 is not incidental, and shows that Navier-Stokes equations, despite shortcomings, capture the essence of the jet's hydrodynamic effect. The TMF geometry and the existence of a ballistic jet consisting of electrons following cyclotron orbits were approximated by injecting carriers at *i* (non-zero $\vec{v}$ normal to the boundary) and extracting the carriers at *c*, located 7 μm removed from *i* along the same boundary (non-zero $\vec{v}$ normal to the boundary, opposite to $\vec{v}$ imposed at *i*) (Fig. 3a main text). In the vicinity of *i* and *c*, the velocity fields of the injected or extracted carriers obtained from the Navier-Stokes equations and the actual velocity fields are not expected to have yet accumulated substantial differences. The potential profiles obtained in the Navier-Stokes solutions for the vicinity of *c* (Fig. 3b main text) are then also anticipated to bear a realistic resemblance to the experimentally expected potential profiles. The expectation of realistic potential profiles is reinforced by the similarity between Fig. 3b main text, and Ref. 19, Fig. 2. Limited-slip boundary conditions (allowing a finite velocity tangential to the boundaries) may change the scale of the potential profiles in the vicinity of the apertures, but leave the overall profile shape relatively unaffected and particularly would mostly preserve the existence of regions of negative potential in the vicinity of the barrier.

S8. Temperature dependence of TMF

As stated in the main text, the decay of TMF amplitudes can be modeled as $\Delta R_f = R_o \exp(-\tau_{tr}/\tau)$ where $\tau^{-1}(T)$ represents the rate of decay of ΔR_f, τ_{tr} is the traversal time and R_o is the value of TMF amplitude in the absence of scattering. By Matthiessen's rule, the total scattering rate $\tau^{-1}(T)$ can be expressed as sum of individual scattering rates corresponding to different scattering mechanisms that can be present in the system. Referring to S6:

$$\frac{1}{\tau(T)} = \frac{1}{\tau_{ee}(T)} + \frac{1}{\tau_e(T)} = \frac{1}{\tau_{ee}(T)} + \frac{1}{\tau_{ph}(T)} + \frac{1}{\tau_{e,o}} \qquad (19)$$

Since our system is extremely pure ($1/\tau_{e,0} \approx 0$) and as is clear from Fig. S6a and Fig. 4e main text, $1/\tau_e < 1/\tau_{ee}$ for the entire range of T, such that we can simplify to:

$$\frac{1}{\tau(T)} \approx \frac{1}{\tau_{ee}(T)} = \frac{(k_B T)^2}{hE_F}\left[\ln\frac{E_F}{k_B T} + \ln\frac{4}{a_o^* k_F} + 1\right]$$

This simplification is valid for TMF analysis but not for analysis of $\mu(T)$, since e-e scattering does not affect μ in pure systems whereas it dominates the decay of TMF. For simplicity, we omit the last two terms in Eq. (15), and introduce a parameter C which can account for their contribution along with the prefactor in Eq. (15). We obtain:

$$\frac{1}{\tau(T)} \approx CT^2 \ln\frac{E_F}{k_B T}$$

At 4.2 K, E_F = 10.9 meV (≈ constant in T), yielding E_F/k_B = 126 K and

$$\frac{1}{\tau(T)} \approx CT^2 \ln\frac{126}{T} \qquad (20)$$

Substituting in ΔR_f, we obtain:

$$\Delta R_f \approx R_o e^{-\tau_{tr} CT^2 \ln\frac{126}{T}}$$

We hence fit the data with:

$$\Delta R_f \approx A e^{-BT^2 \ln\frac{126}{T}} \qquad (21)$$

where $B = \tau_{tr} C$.

Equation S21 provides a very good fit to the experimental data. A yields the value of R_o required for obtaining the extracted decay rate $\tau^{-1}(T)$ and decay length $\ell(T)$. From ΔR_f for G2, we obtain $A = R_o$= 347 Ω and for G4, $A = R_o$= 242 Ω. The parameter B = 0.0129 K^{-2} for G2 and 0.0116 K^{-2} for G4. The difference (~10 %) is small and is attributed to the geometrical differences. We also note that value of B is bit lower for ΔR_p in both the geometries and that is expected because τ_{tr} for the minima (pumping) should be weighted towards shorter trajectories closer to the barrier (Fig. S2c) which result in a stronger pumping effect.

S9. Current dependence of TMF

TMF spectra were obtained at currents I_i ranging from 50 nA to 1 μA rms (Fig. S7a-b) for the G1 geometry. Figure S7a shows that $R_f(B)$ spectra stay noticeably constant for I_i < 400 nA, beyond which

heating effects start playing role and the TMF amplitude decreases with increasing I_i (non-linear regime, Fig. S7b). The linear regime with ΔR_f, ΔR_b and ΔR_p appreciably constant in I_i hence extends up to ~ 400 nA, as shown in Fig. S7b, depicting normalized ΔR_b and ΔR_p plotted vs I_i. The pumping effect (ΔR_p) is expected to show a linear dependence on current if heating effects are avoided, as pointed out in Ref. 19 and as expected since viscous forces are linear in velocity. Bernoulli's equation on the other hand expresses energy conservation for fluids where viscous forces can be neglected, and finds pressure variations quadratic in velocity (via kinetic energy), hence *increasing quadratically* in current. We hence put forward that the *low-current linearity* of the pumping effect observed in our work is an important property that shows hydrodynamic effects and viscosity play a role, and that differentiates it from pumping effects based on energy conservation (which would increase nonlinearly in current).

The linearity is valid only up to the current regime where electron heating effects start playing a role. But the nonlinearity above this current is not intrinsic to the pumping effect, nor to TMF. Comparing the current dependence of ΔR_b (TMF maxima) and ΔR_p (TMF minima) in the non-linear regime, no systematic differences in behavior are apparent (Fig. S7b).

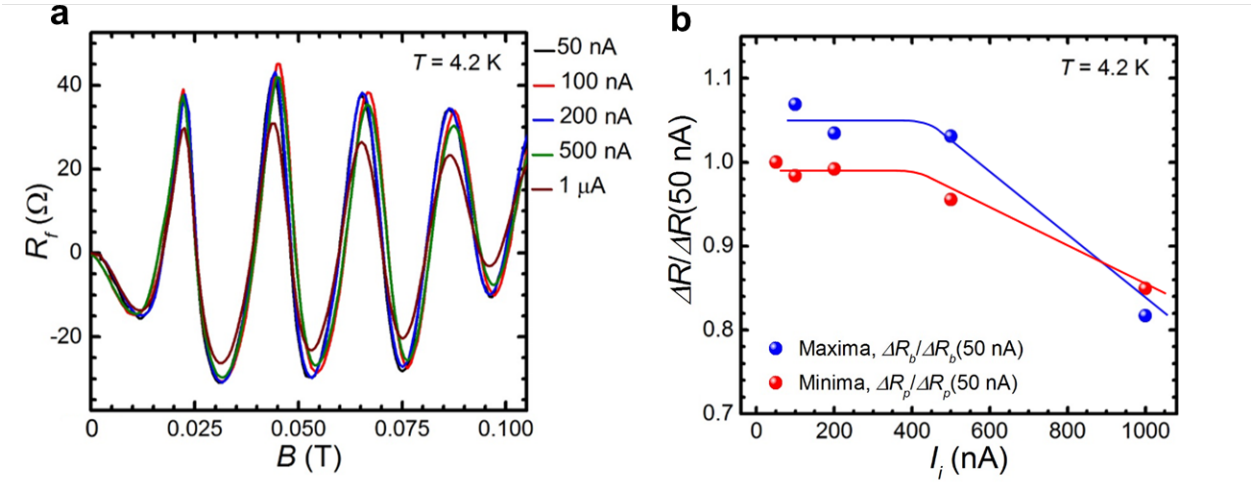

Figure S7| Current dependence of TMF. a, TMF spectra measured at various injected currents in the G1 geometry. **b,** ΔR /ΔR(50nA) plotted vs I_i showing linearity extending up to 400 nA, followed by non-linearity at higher currents. Linearity in current of the pumping effect is another property highlighting the importance of hydrodynamic effects.

References

1. LaGasse, S. W. & Lee, J. U. Understanding magnetic focusing in graphene p−n junctions through quantum modeling. *Phys. Rev. B* **95**, 155433 (2017).
2. Zawadzki, W. & Szymanska, W. Elastic electron scattering in InSb-type semiconductors. *Phys. Stat. Sol. B* **45**, 415 (1971)
3. Zawadzki, W. Semirelativity in semiconductors: a review. *J. Phys.: Condens. Matter* **29**, 373004 (2017).
4. Harris, J.J. *et al.* Acoustic phonon scattering in ultra high mobility, low carrier density GaAs/(Al,Ga)As heterojunctions. *Surface Science* **229**, 113-115 (1990).
5. Onsager, L. Reciprocal relations in irreversible processes. II. *Phys. Rev. B* **38**, 2265-2279 (1931).
6. Casimir, H. B. G. On Onsager's principle of microscopic reversibility. *Rev. Mod. Phys.* **17**, 343-350 (1945).
7. Sanchez, D. & Kang K. Validity and breakdown of Onsager symmetry in mesoscopic conductors interacting with environment. *Phys. Rev. Lett.* **100**, 036806 (2008).
8. Tsoi, V. S. Focusing of electrons in a metal by a transverse magnetic field. *JETP Lett.* **19**, 70-71 (1974).
9. Heremans, J. J., Santos, M. B. & Shayegan, M. Transverse magnetic focusing and dispersion of GaAs 2D holes at (311)A heterojunctions. *Surface Science* **305**, 348-352 (1994).
10. Büttiker, M. Four terminal phase coherent conductance. *Phys. Rev. Lett.* **57**, 1761 (1986).
11. Datta, S. *Electronic Transport in Mesoscopic System* (Cambridge University Press, Cambridge, 1995).
12. Ferry, D. & Goodnick, S. M. *Transport in Nanostructures* (Cambridge University Press, Cambridge, 1997).
13. Beconcini, M. *et al*. Scaling approach to tight-binding transport in realistic graphene devices: The case of transverse magnetic focusing. *Phys. Rev. B* **94**, 115441 (2016).
14. Milivanovic, S. P., Masir, M. R., Peeters, F. M. Magnetic electron focusing and tuning of the electron current with p-n junctions. *Journal of Applied Physics* **115**, 043719 (2014).
15. Beenakker, C. W. G & van Houten, H. Billiard model of a ballistic multiprobe conductor. *Phys. Rev. Lett.* **63**, 1857 (1989).
16. Tarucha, S., Saku, T., Hirayama, Y. & Horikoshi, Y. Bend-resistance characteristics of macroscopic four-terminal devices with a high electron mobility. *Phys. Rev. B* **45**, 13465 (1992).
17. Hackens, B., Gence, L., Gustin, C., Wallart, X., Bollaert, S., Cappy, A. & Bayot, V. Sign reversal and tunable rectification in a ballistic nanojunction. *Appl. Phys. Lett.* **85**, 4508 (2004).

18. Taubert, D. *et al*. An electron jet pump: The Venturi effect of a Fermi liquid. *J. Appl. Phys.* **109**, 102412 (2011).
19. Govorov, A. O. & Heremans, J. J. Hydrodynamic effects in interacting Fermi electron jets. *Phys. Rev. Lett.* **92,** 26803 (2004).
20. Alekseev, P. S. Negative magnetoresistance in viscous flows of two-dimensional electrons. *Phys. Rev. Lett.* **117,** 166601 (2016).
21. Guo, H., Ilseven, E., Falkovich, G. & Levitov, L. Higher-than-ballistic conduction of viscous electron flows. *Proc. Natl Acad. Sci. USA* **114,** 3068–3073 (2017).
22. Torre, I., Tomadin, A., Geim, A. K. & Polini, M. Nonlocal transport and the hydrodynamic shear viscosity in graphene. *Phys. Rev. B* **92,** 165433 (2015).
23. Lucas, A. & Fong, K. C. Hydrodynamics of electrons in graphene. *J. Phys. Cond. Matter* **30,** 053001 (2018).
24. Levitov, L. & Falkovich, G. Electron viscosity, current vortices and negative non local resistance in graphene. *Nature Physics* **12**, 672–676 (2016).
25. de Jong, M .J. M & Molenkamp L. W. Hydrodynamic electron flow in high-mobility wires. *Phys. Rev. B.* **51,** 13389 (1995).
26. Gurzhi, R. N. Hydrodynamic effects in solids at low temperature. *Sovi. Phys. Uspekhi* **11,** 255– 270 (1968).
27. Scaffidi, T., Nandi N., Schmidt, B., Mackenzie, A. P. & Moore J.E. Hydrodynamic electron flow and Hall viscosity. *Phys. Rev. Lett.* **118,** 226601 (2017).
28. Giuliani, G. F. & Quinn, J. J. Lifetime of a quasiparticle in a two-dimensional electron gas. *Phys. Rev. B* **26**, 4421 (1982).
29. Moll, P. J. W., Kushwaha, P., Nandi, N., Schmidt, B. & Mackenzie, A. P. Evidence for hydrodynamic electron flow in PdCoO2. *Science* **351**, 1061 (2016).
30. Lee, M. *et al*. Ballistic miniband conduction in a graphene superlattice. *Science* **353**, 1526 (2018).
31. Chandra, M., Kataria, G., Sahdev, D. & Sundararaman, R. Hydrodynamic and ballistic AC transport in two-dimensional Fermi liquids. *Phys. Rev. B* **99**, 165409 (2019).